IET Intelligent Transport Systems

Research Article

IET Journals
The Institution of Engineering and Technology

ISSN 1751-8644
doi: 0000000000
www.ietdl.org

Millimetre-wave Massive MIMO for Cellular Vehicle-to-Infrastructure (C-V2I) Communication

Sherif Adeshina Busari[1*], *Muhammad Awais Khan*[1], *Kazi Mohammed Saidul Huq*[1], *Shahid Mumtaz*[1], *Jonathan Rodriguez*[1,2]

[1] *Instituto de Telecomunicações, 3810-193, Aveiro, Portugal*
[2] *University of South Wales, Pontypridd, CF37 1DL, United Kingdom*
** E-mail: sherifbusari@av.it.pt*

Abstract: Autonomous driving is delightedly an innovative and revolutionary paradigm for future intelligent transport systems (ITS). To be fully-functional and efficient, vehicles will use hundreds of sensors and generate terabytes of data that will be used and shared for safety, infotainment and allied services. Communication among vehicles or between vehicle and infrastructure thus requires data rate, latency and reliability far beyond what the legacy dedicated short range communication (DSRC) and Long Term Evolution- Advanced (LTE-A) systems can support. In this work, we motivate the use of millimetre-wave (mmWave) massive multiple-input multiple-output (MIMO) technology to facilitate gigabits-per-second (Gbps) communication for cellular vehicle-to-infrastructure (C-V2I) scenarios. As a fundamental component, we characterize the mmWave massive MIMO vehicular channel using metrics such as path loss, root-mean-square delay spread, Rician K-factor, cluster and ray distribution, power delay profile, channel rank and condition number as well as data rate. We compare the mmWave performance with the DSRC and LTE-A capabilities, and offer useful insights on vehicular channels. Our results show that mmWave massive MIMO can deliver Gbps data rates for next-generation vehicular networks.

1 Introduction

The recent partnership of the automotive and telecommunications industries in the area of intelligent transport systems (ITS) aims to evolve innovative technology solutions for next-generation vehicular networks (NGVNs). The 5G Automotive Association (5GAA) is driving a unified framework for the realization and commercialization of the fifth-generation new radio cellular vehicle-to-everything (5G NR C-V2X) paradigm, where X could be anything: another vehicle (V2V), infrastructure (V2I), network (V2N), device (V2D), grid (V2G) or even person/pedestrians (V2P). While the third generation partnership project (3GPP) has standardized C-V2X in its Release 14, the extension to support 5G NR is anticipated to be finalized in Release 16 for more advanced use cases [1].

Currently, the dedicated short range communication (DSRC) (known as ITS-G5 in Europe) is the legacy system for vehicular communication and safety. It operates on the 5.9 GHz band using transceivers based on the IEEE 802.11p standard [2]. DSRC algorithms and protocols have been tested in field trials around the world by different industries and equipment vendors. Recently, a start-up named Virtual Traffic Light (VTL) implemented and publicly trialled an algorithm which enables vehicles to control and coordinate their traffic using exchanged DSRC-based safety messages without the need for traffic lights or human interventions. The algorithm operates on the leader-follower concept in a round robin fashion. The participating vehicles share both benefits and responsibilities in order to ensure fairness. Today, vehicles with DSRC chipsets have started to hit the market and are expected to be widely available soon [3].

Unfortunately, DSRC can only support data rates up to 27 Mbps, with typical average of 2-6 Mbps. This is grossly inadequate for NGVNs foreseen to require multi-gigabits-per-second (Gbps) rates. To address this concern, many researchers have advocated the adoption of the 3GPP's Long Term Evolution-Advanced (LTE-A) for vehicular communication. However, this fourth-generation (4G) system can only support a maximum data rate of 100 Mbps in high mobility (vehicular) scenarios. The same story goes for the bandwidth, reliability and latency requirements [4]. Consequently, the industrial and academic research communities have identified the millimetre-wave (mmWave) bands to come to the rescue [2, 5, 6].

Fortunately, the mmWave bands are being extensively explored for 5G services and applications due to their amazing spectral prospects. The mmWave bands (24.25-300 GHz [7] or 30-300 GHz [8]) have very large bandwidths that can support high-rate, low-latency and massive connectivity required for vehicular applications such as the connected autonomous vehicles (CAVs) [6]. These requirements correspond to the enhanced mobile broadband (eMBB), ultra-reliable and low-latency communications (URLLC) and massive machine type communications (mMTC) use cases to be supported by 5G as well [9]. More so, the use of the mmWave bands in standardized systems such as IEEE 802.11ad (60 GHz) and radar systems (76 GHz) gives additional green light [5].

1.1 Potential Applications of C-V2X

Alongside the delight of self-driving vehicles, NGVNs will facilitate newer use cases in infrastructure-assisted and autonomous driving and enable high-rate infotainment and ultra-reliable safety services. This is in addition to the anticipated benefits of enhanced vehicular safety, better traffic management, more efficient toll collection and commute time reduction, among others. Thus, ITS-supported vehicles will be equipped with tens to hundreds of sensors (e.g., LIDAR, ultrasonic, radar, camera, etc.) which together with the on-board communication chipsets will enable diverse services, using any or a combination of the V2X paradigms [2, 5, 6].

For V2I links (illustrated in Fig. 1 on the next page), the infrastructure can gather sensing data (about the vehicles or the surrounding traffic) from the vehicles. The sensed data can be processed in the cloud and used to provide live images or real-time maps of the environment. These maps can be used by the transportation control system for congestion avoidance, general warnings (such as dangerous situations) and overall traffic efficiency improvement. Also, automakers can use the sensed data for fault or potential failure diagnosis of the vehicles. The infrastructure can also be used to provide high rate internet access to the vehicles for automated driving and

infotainment services such as media download and video streaming [1, 5].

Similarly, the potential V2V applications include cooperative perception where perceptual data from from neighbouring vehicles can be used to create a satellite view of the surrounding traffic. The view can be used to extend the perception range of the vehicles in order to reveal hidden objects, cover blind spots and avoid collision. Shared data among the vehicles can also be used for other applications such as path planning and trajectory sharing, among others [2, 5]. For details on the potential applications of Gbps vehicular communications (V2I and V2V), see chapter 3 of [5].

1.2 Related Works

While the prospect of 5G NR C-V2X is amazing, the mmWave channel exhibits challenging propagation properties markedly different from the sub-6 GHz channels where both DSRC and LTE-A operate [10–13]. The differences become even more pronounced for mmWave vehicular channels due to the impact of high mobility [2, 5, 14]. Many authors have attempted to address different aspects of the challenges. Majority of the works centre on the V2V and V2I scenarios in urban street [15–17], highway [2, 6] and high speed rail (HSR) [18, 19] environments. The works on V2I consider the infrastructures as base stations (BSs) or small cells (SCs) with typical range 200-500 m, which translate to sub-6 GHz and mmWave channels with many clustered blockers and scatterers and where models such as [20, 21] can be readily adopted. However, [21] does not consider mobility while [20] supports only pedestrian mobility and is reported to have excessive number of clusters and sub-paths that is unsupported by measurement [22].

In this work, however, we motivate the use of mmWave massive MIMO for Gbps vehicular communication. Here, the mmWave massive MIMO access points (APs) are mounted on street lampposts spaced at very short intervals, typically 20 m for dense road side unit (RSU) deployment [5]. We then characterize the mmWave vehicular channel and compare its performance with the DSRC and LTE-A (sub-6 GHz) vehicular channel. To the authors' best knowledge, this work is the first to characterize this future ITS scenario using 5G NR C-V2I. We note in advance that we focus on the downlink (i.e., I2V) set-up in this work. However, we use V2I throughout this article in order to conform to the V2X convention for the sake of consistency.

The remainder of this paper is organized as follows. In Section 2, we present the system model and describe the network layout, channel model, antenna configurations and precoding technique employed. In Section 3, we provide the evaluation metrics and parameters used for performance assessment. Results and discussions follow in Section 4, while the conclusion and future research direction are presented in Section 5.

2 System Model

In this section, we present the network layout, antenna and channel models as well as the precoding technique employed.

2.1 Network Deployment

We show in Fig. 1 the system layout for a downlink C-V2I. We consider a $d_r = 500$ m-long section of the road in an urban microcellular (UMi) environment. Stationary APs are mounted at height $h_{TX} = 5$ m on street lampposts with a density of $\Omega_{TX} = 50$ BS/km. This corresponds to 25 evenly-spaced APs for the considered distance. The vehicles traverse the route at a speed of $v_{RX} = 36$ km/h $= 10$ m/s, and have roof-mount antennas with height $h_{RX} = 1.5$ m above the reference ground level.

Further to the described layout, we assume that the APs are connected by high rate backhaul links. Downlink connectivity is by LOS with the roof-top positioning of vehicle antennas. Therefore, the relatively high position of the APs (compared to a V2V scenario) ensures good link [23]. Also, the three-dimensional (3D) separation distance d_{3D} between the vehicle (RX) and its serving AP (TX) at

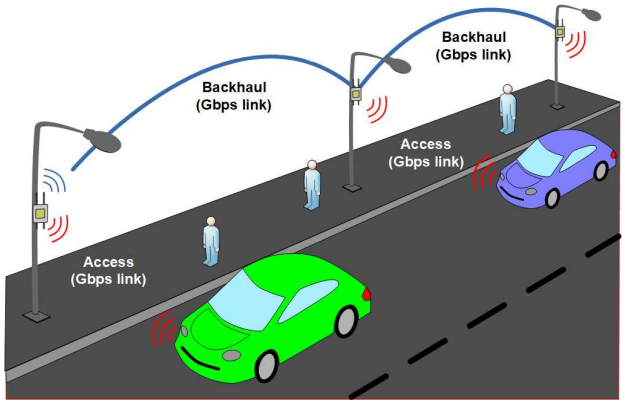

Fig. 1: Network deployment layout

each time instant of the considered scenario gives a line of sight (LOS) probability $P_{LOS} \approx 1$, according to (1) [24].

$$P_{\mathrm{LOS}}(d_{3D}) = \left[\min\left(\frac{27}{d}, 1\right)\left(1 - e^{-\frac{d}{71}}\right) + e^{-\frac{d}{71}}\right]^2 \quad (1)$$

As a result, V2I communication in this scenario is by LOS. It should be noted that LOS here does not mean pure LOS as there is still sparse blockage and scattering effects from pedestrians, trees and road signs.

2.2 Channel Model

We consider a clustered 3D statistical spatial channel model (SSCM) for the considered V2I channel. The effective (omnidirectional) path loss PL_{eff}, which combines the path loss (PL) and the shadow fading (SF), is given by (2) and (3).

$$PL_{eff} = PL + SF \quad (2)$$

$$PL_{eff} = 20\log_{10}\left(\frac{4\pi f_c}{c}\right) + 10\bar{n}\log_{10}(d_{3D}) + X(0,\sigma) \quad (3)$$

where $\bar{n}$ is the path loss exponent (PLE) and X is the log-normal random SF variable with zero mean and σ standard deviation [24, 25]. We note that blockage is modelled inherently in (3) as it matches the blockage-dependent PL model (4) in [24] when there is randi(0,1) number of blockers at each time instant. This appropriately models the LOS and sparse blockage regime of the considered scenario.

$$PL = 10\kappa\log_{10}(d_{3D}) + \Upsilon + 15\left(\frac{d_{3D}}{1000}\right) \quad (4)$$

where κ and Υ are parameters determined by the number of blockers (see [5], Table 7.2).

The fast-fading double-directional channel impulse response (CIR) h_{dir} with N_{cl} clusters and N_{sp} subpaths/rays/multipath component (MPC) per cluster for each transmission link is given by (5) (at the top of next page). The $P_{RX,c,s)}$, $\varphi_{c,s}$ and $\tau_{c,s}$ in (5) denote the received power magnitude, phase and propagation time delay of the cluster-subpath combinations, respectively. The parameter t is time while ϕ and θ represent the angle offsets from the boresight direction for the azimuth and elevation, respectively. For each ray, $\phi_{c,s}$ and $\theta_{c,s}$ are the azimuth angle of departure (AAoD) and elevation angle of departure (EAoD) at the AP, and azimuth angle of arrival (AAoA) and elevation angle of arrival (EAoA) for the vehicle, as the case may be. Also, G_{TX} and G_{RX} are the transmit and receive antenna gains modelled as in (6) and (7) [24, 25].

$$h_{dir}(t,\phi,\theta)=\sum_{c=1}^{N_{cl}}\sum_{s=1}^{N_{sp,c}} P_{RX,c,s}\cdot e^{j\varphi_{c,s}}\cdot\delta(t-\tau_{c,s})\cdot G_{TX}(\phi-\phi_{c,s},\theta-\theta_{c,s})\cdot G_{RX}(\phi-\phi_{c,s},\theta-\theta_{s,t}) \tag{5}$$

$$\mathbf{H}=\frac{N_{RX}N_{TX}}{\sum_{c=1}^{N_{cl}}N_{sp,c}}\cdot\sum_{c=1}^{N_{cl}}\sum_{s=1}^{N_{sp,c}}\sqrt{PL_{c,s(d_{c,s})}}\cdot e^{j2\pi\left(f_c\tau_{c,s}+\frac{v_{RX}\cos(\phi_{c,s})}{\lambda}\triangle t\right)}\cdot\mathbf{a}_{RX}\left(\phi_{c,s}^{RX}\right)\mathbf{a}_{TX}^{H}\left(\phi_{c,s}^{TX}\right) \tag{11}$$

$$\mathbf{a}_{RX}\left(\phi_{c,s}^{RX}\right)=\frac{1}{\sqrt{N_{RX}}}\begin{pmatrix} e^{j\frac{2\pi}{\lambda}d_{RX}(n_r-1)\sin\left(\phi_{c,s}^{RX}\right)}\end{pmatrix},\qquad \forall n_r=1,2,...,N_{RX} \tag{12}$$

$$\mathbf{a}_{TX}\left(\phi_{c,s}^{TX}\right)=\frac{1}{\sqrt{N_{TX}}}\begin{pmatrix} e^{j\frac{2\pi}{\lambda}d_{TX}(n_t-1)\sin\left(\phi_{c,s}^{TX}\right)}\end{pmatrix},\qquad \forall n_t=1,2,...,N_{TX} \tag{13}$$

$$\tau_{RMS}=\sqrt{\frac{\sum_{c=1}^{N_{cl}}\sum_{s=1}^{N_{sp,c}}\tau_{c,s}^2P_{RX,c,s}}{\sum_{c=1}^{N_{cl}}\sum_{s=1}^{N_{sp,c}}P_{RX,c,s}}-\left(\frac{\sum_{c=1}^{N_{cl}}\sum_{s=1}^{N_{sp,c}}\tau_{c,s}P_{RX,c,s}}{\sum_{c=1}^{N_{cl}}\sum_{s=1}^{N_{sp,c}}P_{RX,c,s}}\right)^2} \tag{14}$$

$$G(\phi,\theta)=\max\left(G_0e^{\alpha\phi^2+\beta\theta^2},\frac{G_0}{100}\right) \tag{6}$$

$$\alpha=\frac{4\ln(2)}{\phi_{3dB}^2},\quad \beta=\frac{4\ln(2)}{\theta_{3dB}^2},\quad G_0=\frac{41253\xi}{\phi_{3dB}^2\theta_{3dB}^2} \tag{7}$$

where G_0 is the maximum directive boresight gain, ξ is the average antenna efficiency, ϕ_{3dB} and θ_{3dB} are the azimuth and elevation half-power beamwidths (HPBW), respectively. The variables α and β are evaluated using (7).

It should be noted that due to the high vehicular mobility (relative to static and pedestrian cases), the channel becomes time-variant (i.e., the channel coherence time becomes smaller than the observation window). The resulting phase $\varphi_{c,s}$, given by (8)-(10), is now composed of the distance-dependent phase change $\Theta_{c,s}$ and the velocity-induced Doppler shift $\vartheta_{D(c,s)}$ (caused by the Doppler frequency due to the relative motion between the TX and RX) .

$$\varphi_{c,s}=\Theta_{c,s}+\vartheta_{D(c,s)} \tag{8}$$

$$\varphi_{c,s}=2\pi\left(f_c\tau_{c,s}+f_{D(c,s)}\triangle t\right) \tag{9}$$

$$\varphi_{c,s}=2\pi\left(f_c\tau_{c,s}+\frac{v_{RX}\cos(\phi_{c,s})}{\lambda}\triangle t\right) \tag{10}$$

where $f_{D(c,s)}$ is the Doppler frequency which is positive when the vehicle is moving towards the AP and negative when moving away from it [26, 27].

2.3 Antenna Model and Precoding

The APs and vehicles are equipped with massive MIMO arrays with N_{TX} and N_{RX} antenna elements, respectively. We consider uniform linear arrays (ULAs) with inter-element spacing $d_{TX}=d_{RX}=\lambda/2$, where $\lambda=c/f_c$ is the wavelength ($c=3\times10^8$ m/s is the speed of light and f_c is the carrier frequency). For massive MIMO, the CIR $h_{dir}(t,\phi,\theta)$ in (5)-(10) is extended to the channel matrix $\mathbf{H}(N_{RX}\times N_{TX})$ in (11), where $\mathbf{a}_{RX}$ and $\mathbf{a}_{TX}$ are the RX and TX array response (or steering) vectors for ULA given by (12) and (13), respectively [8] (see top of page for (11)-(13)).

DSRC and LTE-A use limited numbers of antenna elements. Typical MIMO configurations are 2×2, 2×4, 4×4 and 2×8 for $N_{RX}\times N_{TX}$. On the other hand, mmWave massive MIMO arrays employ large number of antenna elements. At 70 GHz, for example, the arrays can go up to 64×1024 (with typical configurations being 16×64, 16×128 and 32×256 for $N_{RX}\times N_{TX}$) according to the 3GPP. The maximum number of radio frequency (RF) chains or number of streams at the RX and TX at such frequency are 8 and 32, respectively [8, 9, 11, 28]. The large arrays offer amazing opportunities to beamform highly-directive beams (through analogue beamforming) or multiplex multiple streams (via digital and hybrid precoding) for high data rates. Many studies advocate for hybrid precoding for mmWave massive MIMO for its balanced trade-off between spectral efficiency (SE) and energy efficiency (SE), relative to the power-exhaustive digital precoding and the low-rate analogue beamforming [8, 25, 29].

We note that the APs and vehicles in the considered vehicular scenario are not power constrained (due to the seemingly unlimited energy from the lamppost and vehicle battery, respectively. However, we employ analogue beamforming for two reasons. First, the short TX-RX separation distance, LOS propagation [25] and high level of antenna correlation due to single-user (SU) MIMO and sparse scattering [30] potentially guarantees near-optimal performance with analogue beamforming. Second, single-stream beamforming ensures a fair comparison of performance of the mmWave massive MIMO with the DSRC and LTE-A that use modest number of antennas.

3 Performance Metrics

To compare the performance of DSRC and LTE-A with the mmWave massive MIMO advocated in this work, we characterize the vehicular channel using PL, root-mean-square delay spread (τ_{RMS}), Rician K-factor (KF), number of clusters, number of resolvable MPCs/rays/subpaths, power delay profile (PDP), channel rank, channel condition number and data rate (R). For the analysis, PL is evaluated using (3) in subsection 2.2 while the RMS delay spread τ_{RMS} is evaluated using (14) [31] (shown on top of page). The Rician KF is evaluated using (15) [32].

Table 1 Key Simulation Parameters

Parameter	DSRC	LTE-A	mmWave
f_c (GHz)	5.9	2.6	73
BW (MHz)	10	20	396
N_{TX}	2	4	64
N_{RX}	2	4	16
ϕ_{3dB}^{TX}	65°	65°	10°
ϕ_{3dB}^{RX}	65°	65°	10°

$$KF = \frac{P_{RX,c=1,s=1}}{\left(\sum_{c=1}^{N_{cl}} \sum_{s=1}^{N_{sp,c}} P_{RX,c,s}\right) - P_{RX,c=1,s=1}} \quad (15)$$

where the numerator in (15) is the LOS component (P_{LOS}) and the denominator is the sum of all NLOS components ($\sum P_{NLOS}$).

The number of clusters (N_{cl}) and subpaths per cluster ($N_{sp,c}$) are randomly generated as uniform discrete distributions. The cluster (and subpaths) powers, delays and phases follow lognormal, exponential and uniform $(0, 2\pi)$ distributions, respectively [24]. The channel rank gives the measure of how many data streams can be multiplexed while the channel condition number is an indicator for the quality of the wireless channel [21]. The transceivers use $N_{TX}^{RF} = N_{RX}^{RF} = 1$ RF chain for the analogue beamforming processing considered. The precoding and combining matrices thus reduce to vectors $\mathbf{f} \in \mathbb{C}^{N_{TX} \times 1}$ and $\mathbf{w} \in \mathbb{C}^{N_{RX} \times 1}$, respectively. The channel matrix $\mathbf{H}(N_{RX} \times N_{TX})$ used in this work as stated in Table 1, is 2×2, 4×4 and 16×64, for DSRC, LTE-A and mmWave, respectively. The received signal, y, is then given by (16).

$$y = \sqrt{\rho}\mathbf{w}^* \mathbf{H}\mathbf{f}s + \mathbf{w}^* n \quad (16)$$

where ρ is the average received power, $n = N_o \cdot BW \cdot NF$ is the noise (N_o is the noise power spectral density, BW is bandwidth and NF is the noise figure). The achievable data rate/throughput is given by (17).

$$R = BW \cdot \log_2 \left(1 + \rho R_n^{-1} \mathbf{w}^* \mathbf{H}\mathbf{f} \times \mathbf{f}^* \mathbf{H}\mathbf{w}\right) \quad (17)$$

where $R_n = \sigma_n^2 \mathbf{w}^* \mathbf{w}$ is the noise covariance after combining and $(\cdot)^*$ denote the conjugate transpose operator.

4 Simulation Results

In this section, we present the simulation results for the three considered technologies using the metrics outlined in Section 3. We simulate for 50,000 transmission time intervals (TTIs) and average results over 100 channel realizations. For fair comparison, we set $NF = 6$ dB, $N_o = -174$ dBm/Hz, transmit power ($P_{TX} = 30$) dBm and PLE $\bar{n} = 2$ for all three systems. The technology-dependent key simulation parameters are given in Table 1.

4.1 Path Loss

The cumulative distribution functions (CDFs) of the omnidirectional effective path loss PL_{eff} (i.e., PL + SF) results for the three technologies are shown in Fig. 2. As can be deduced from (3), PL_{eff} expectedly increases with increasing f_c. Hence, the mmWave system at 73 GHz exhibits a penalty of up to 30 dB of omnidirectional PL, compared to the sub-6 GHz DSRC and LTE-A at 5.9 GHz and 2.6 GHz, respectively. However, the mmWave system compensates for its high PL with large beamforming gains from the highly-directive antenna arrays in order to bring the received powers to levels comparable to or even higher than those of sub-6 GHz systems [5, 30].

In Fig. 3, we show the PL variations as a function of the distance travelled for one AP-vehicle connection time for the three systems,

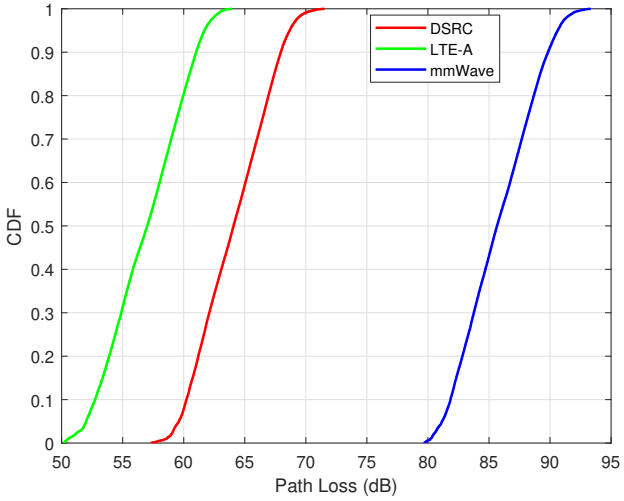

Fig. 2: CDFs of path loss for the three technologies

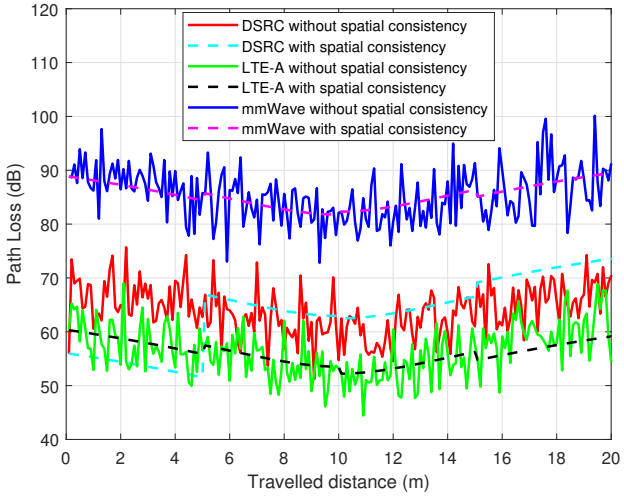

Fig. 3: Path loss variation for the coverage area of one AP

with and without spatial consistency. Similarly, the PL variations as a function of the distance for the entire 500 m route is shown in Fig. 4. It should be noted that the results Fig. 4 are periodic in nature due to inter-AP handovers as the vehicle moves towards and away from the coverage area of each of the densely deployed APs.

As shown in the Figs. 3 and 4, PL variation is random without spatial consistency, due to the impact of SF. With spatial consistency, the variation is more uniform and systematic. We note that it is important for channel models to incorporate spatial consistency where the channel parameters vary in a realistic and continuous manner as a function of position, and by which closely-placed users have similar channel characteristics as against randomized values [33, 34]. We, however, note that large-scale parameters (LSPs) such as SF (and as consequence PL_{eff}) vary more slowly than the fast-fading small-scale parameters (SSPs).

The spatial consistency phenomenon leads to three time scales: channel correlation time (T_c) for LSPs, channel update time (T_u) for SSPs, and then the data transmission time (T_t) for scheduling. The three time scales are related by (18).

$$T_c = \chi \cdot T_u = \chi \cdot \varepsilon \cdot T_t \quad (18)$$

where χ and ε are integer values. We note further that T_t is standardized as 1 ms for 4G and 5G systems. However, it is more realistic for channel-aware schedulers to employ T_u that is used for updating the fast-fading channel parameters as the basis for scheduling. Inspired

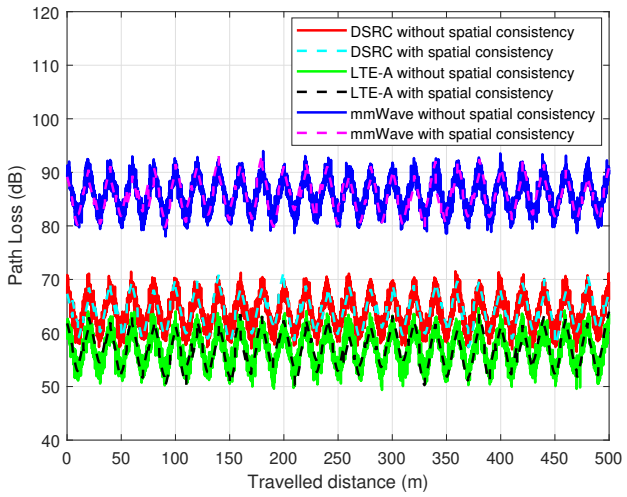

Fig. 4: Path loss variation for the entire route

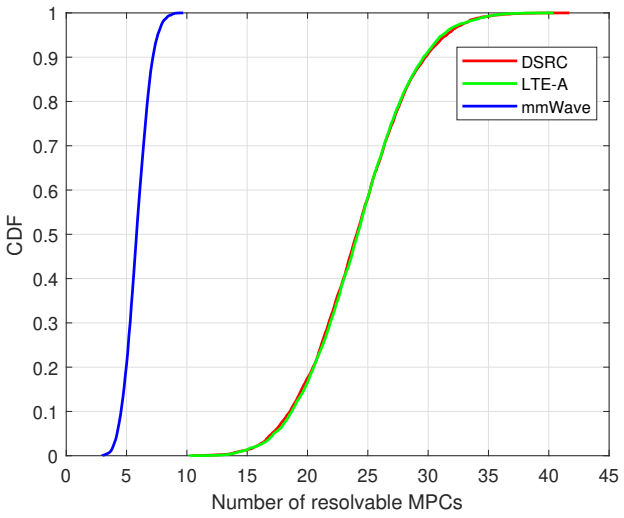

Fig. 6: CDFs for the number of MPCs

by [2, 14, 20, 33], we adopt 0.1 m and 1 m as the update and correlation distances, respectively. At $v_{RX} = 10$ m/s (employed in this work), this corresponds to $\chi = 10$ and $\varepsilon = 10$. Therefore, $T_u = 10$ TTIs $= 10$ ms and $T_c = 100$ TTIs $= 100$ ms.

4.2 Number of Clusters and Sub-paths

The CDFs for the number of clusters and MPCs are shown in Figs. 5 and 6, respectively. Fig. 5 shows that for the considered scenario, the mmWave system has two clusters on the average while the DSRC and LTE-A systems have between 3 and 4 clusters on the average. Similarly, as shown in Fig. 6, the mmWave system has 6 subpaths while DSRC and LTE-A both have 24 subpaths, for the 50% CDF points. On the maximum, the number of subpaths/rays are 9, 40 and 42 for mmWave, LTE-A and DSRC, respectively.

Fig. 6 shows that the mmWave system has limited number of resolvable MPCs compared to the sub-6 GHz propagation. This outcome buttresses the sparse nature of mmWave systems [25]. We note that for longer link distances, the number of clusters and rays will likely increase as more scatterers will likely be encountered.

4.3 Power Delay Profile

In Figs. 7 and 8, we show two snapshots of the PDPs for the three systems considered. PDPs show the distribution of the received signal powers of the MPCs with their corresponding time delays. PDPs

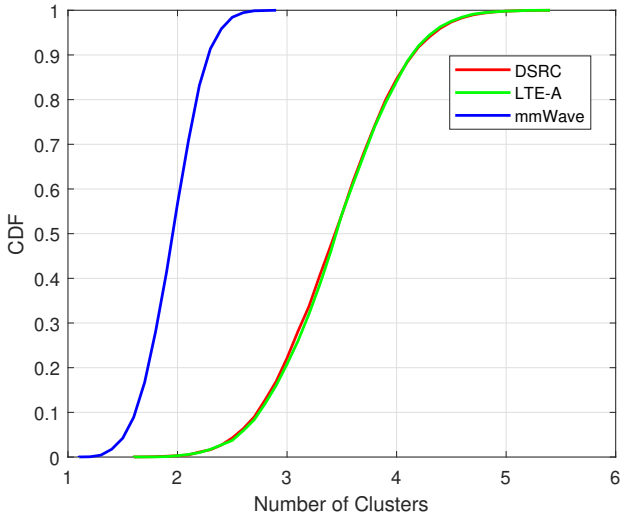

Fig. 5: CDFs for the number of clusters

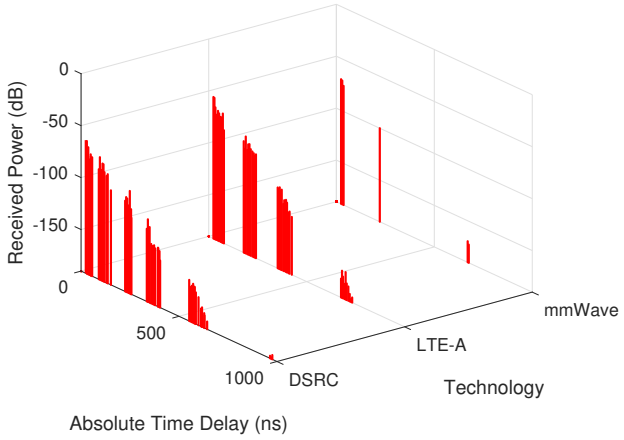

Fig. 7: Power Delay Profile snapshot from n^{th} AP

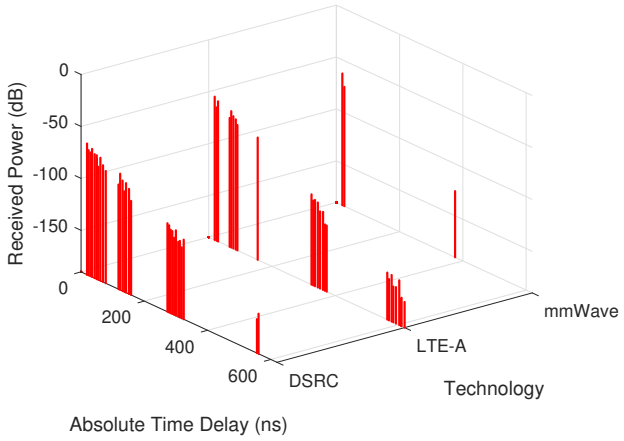

Fig. 8: Power Delay Profile snapshot from m^{th} AP

are also used to characterize the channel with respect to the delay spread and coherence bandwidth [31]. From Figs. 7 and 8, it can be observed that mmWave has lower number of clusters and overall number of rays when compared to the sub-6 GHz DSRC and LTE-A (as earlier shown in Figs.5 and 6).

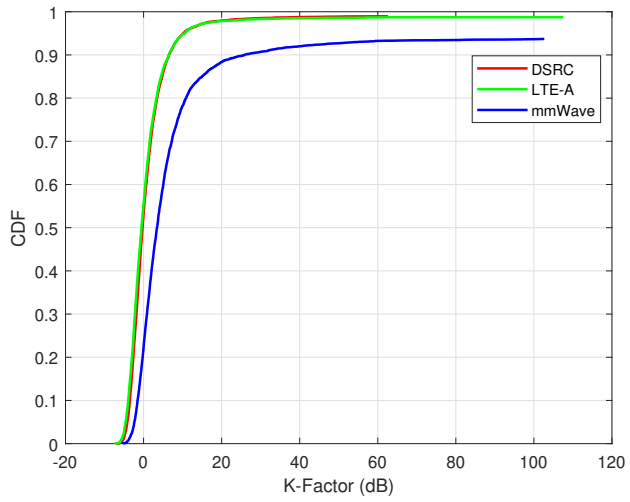

Fig. 9: CDF of K-Factor for the three systems

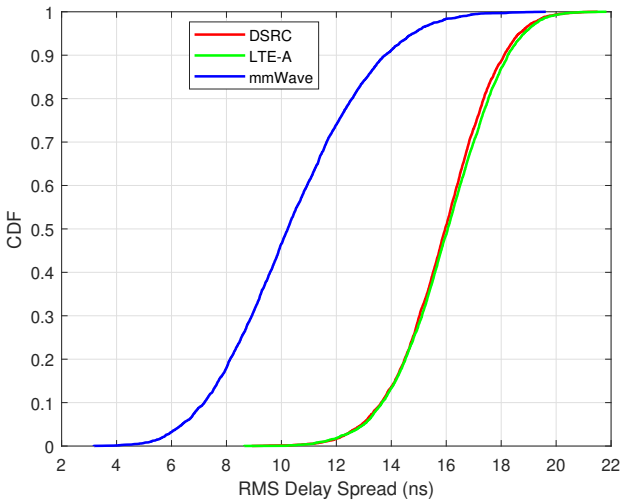

Fig. 10: CDF of RMS Delay Spread

4.4 Rician K-Factor

The Rician K-Factor (KF) statistics is a measure of the ratio of LOS-to-NLOS strength and its value affects the performance of MIMO systems significantly [32]. The presence of LOS component translates to stronger propagation and larger signal to noise ratio (SNR) [22]. Fig. 9 shows the K-Factor CDFs evaluated using (15). It can be readily seen that mmWave has higher KF values than DSRC and LTE-A. This indicates larger LOS strength and higher directivity.

Fig. 9 also shows that the powers of NLOS components dominate only about 20% of time (at 0.2 CDF points) where the K-Factor is less than 0 dB while for the remaining 80%, LOS component dominates. It can also be observed that the curves do not reach the 100% CDF points. The gaps indicate the percentage of pure LOS where only the LOS component is present (i.e., $KF = \infty$ when $\sum P_{NLOS} = 0$). Fig. 8 shows that mmWave has higher percentage of pure LOS than the DSRC and LTE-A as can be seen at the saturation points of the CDF curves.

4.5 Root-Mean-Square Delay Spread

The root-mean-square delay spread τ_{RMS} is a measure of the delay dispersion of the channel. It is evaluated using (14). It is also related to the channel coherence bandwidth B_c which characterizes the frequency selectivity of the channel. If $B_c \ll BW$ (as is the case in wideband systems like mmWave), the channel will be frequency-selective thereby leading to inter-symbol interference (ISI). To combat this, orthogonal frequency division multiplexing (OFDM) is employed in 4G and 5G systems to convert the frequency-selective wideband channels to flat-fading channels. The relationship between τ_{RMS} and B_c is given by (19).

$$B_c \approx \frac{1}{2\pi\tau_{RMS}} \tag{19}$$

The CDFs for the τ_{RMS} for the three systems are shown in Fig. 10. The mmWave system has lower τ_{RMS} due to its narrower beams. According to [5, 14], highly-directive narrow beams can reduce both the delay and Doppler spreads and increase the coherence time in mmWave channels. This resulting outcome lessens the severity of the impact of Doppler spread. More so, the values from the τ_{RMS} CDFs in Fig. 10 when plugged into (19) gives B_c within the range [7, 160] MHz which are far higher than the 156.25 kHz [35], 180 kHz [36, 37] and 1.44 MHz [38] for one OFDM resource block (RB) for DSRC, LTE-A and mmWave (5G NR), respectively. Similarly, the values of τ_{RMS} which fall within the range [1, 22] ns in Fig. 10 are far lesser than the OFDM cyclic prefix (CP) duration of 1.6 μs [35], 5.2 μs [36] and 4.4 μs / 0.57 μs [38] for the DSRC, LTE-A and mmWave (5G NR) standards, respectively. Therefore, ISI is no problem with OFDM as the CP duration is larger than the delay spread.

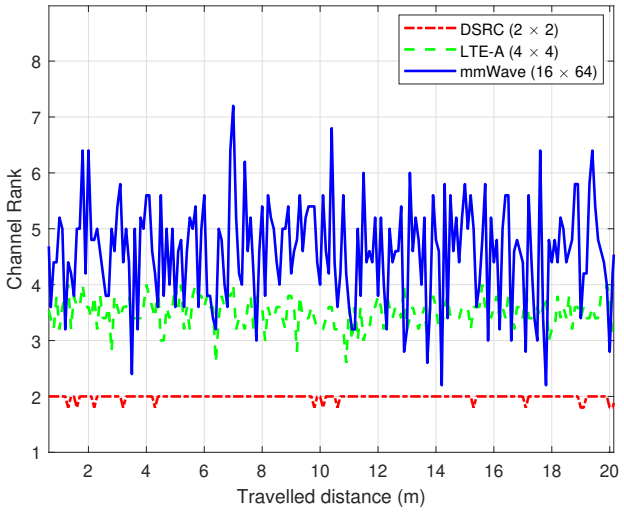

Fig. 11: Channel Rank

4.6 Channel Rank and Condition Number

The rank of a channel matrix determines how many data streams can be sent across the channel. A full rank channel, for example, has $rank = min(N_{RX}, N_{TX})$. While the channel rank is a pointer to the quantitative multiplexing capacity of the channel, it does not indicate the relative strength of the streams. On the other hand, the condition number (CN) is the qualitative measure of the MIMO channel. Using the singular values of the channel matrix, CN indicates the ratio of the maximum to minimum singular values resulting from the singular value decomposition (SVD) of the channel matrix. A channel with $CN = 0$ dB has full rank and thus has equal gains across the channel eigenmodes. With $0 < CN \leq 20$ dB, the channel is rank-deficient with comparable gains across the eigenmodes while $CN > 20$ dB shows that the minimum singular value is close to zero [21].

In Figs. 11 and 12, we show the variations of channel rank and condition number, respectively, with the indicated MIMO configurations. Connecting Figs. 11 and 12, DSRC with rank 2 has $0 < CN \leq 40$ dB. With the relative variation around 20 dB, the channel strengths of the two eigenvalues are comparable. Thus, two streams can be multiplexed over the channel. Optimal performance can be achieved if water-filling algorithm is employed to allocate power to

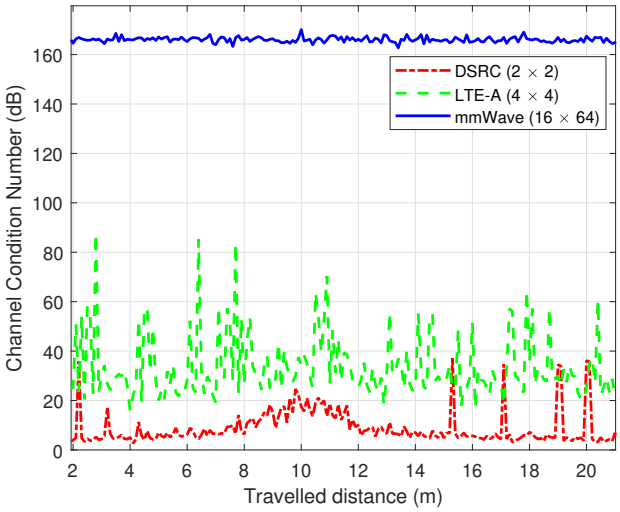

Fig. 12: Channel Condition Number

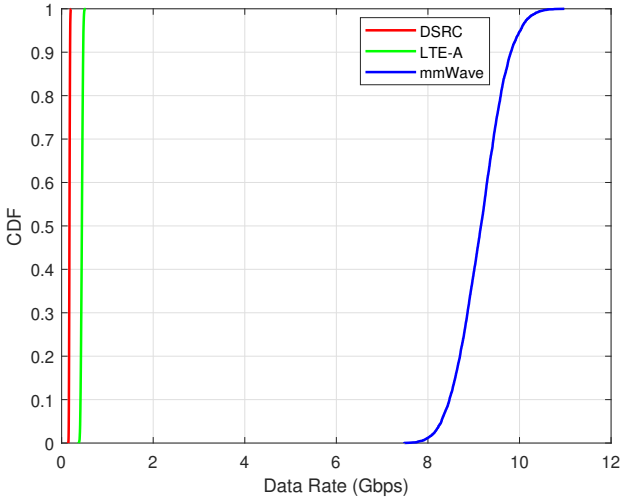

Fig. 13: Data Rate

each of the two streams based on its relative strength. For LTE-A with 4×4 channel, the rank varies between 3 and 4 while the CN is typically higher than 20 dB. This indicates that the number of streams to transmit should not be more than the channel rank for good performance.

Similarly, the mmWave massive MIMO system with 16×64 antenna configuration has rapid fluctuations in rank between 3 and 7 as shown in Fig. 11. However, its extremely high condition number (i.e., $CN > 160$ dB) as shown in Fig. 12 suggests that there are relatively few dominant eigenmodes, far less than 16 (according to $rank = min\,(N_{RX}, N_{TX})$). This results from the high correlation of the tightly-spaced antennas at mmWave, as antenna spacing at 73 GHz mmWave is more than $12\times$ and $24\times$ smaller than at 5. 9 GHz DSRC and 2.6 GHz LTE-A, respectively. This outcome reveals the rank deficiency of mmWave SU-MIMO where single-stream beamforming or precoding with just a few streams per user (depending on the channel rank) gives better performance than precoding with very many streams per user.

4.7 Data Rate

The data rate CDFs of the three systems are shown in Fig. 13. The performance is based on their respective baseline values according to the operating standards. While a direct comparison is unrealistic as we employed different configurations (i.e., with respect to antenna, bandwidth, etc) for the three systems, the results in Fig. 13 motivates the use mmWave massive MIMO for Gbps vehicular communication, particularly for 5G NR C-V2I investigated in this work.

The data rates in Fig. 13 results from using BW of 10, 20 and 396 MHz for DSRC [35], LTE-A [36] and mmWave [38], respectively (see Table 1 in Section 3). It is instructive to note that all the three systems employed single-stream beamforming. The rate is evaluated using (17) and consistently shows the mmWave massive MIMO system achieving multi-Gbps rates, compared to the DSRC and LTE-A (both with less than 500 Mbps). It is instructive to note that the data rates for DSRC and LTE-A shown in Fig. 13 are higher than the values reported in the literature where longer link distance and multi-user MIMO scenarios are typically employed.

5 Conclusion

In this paper, we have characterized the vehicular channel for C-V2I communication where the infrastructure are APs mount on street lampposts in urban street environment. Using diverse channel metrics, we compared the channel statistics of C-V2I using mmWave massive MIMO with that of legacy DSRC and LTE-A systems. With modest system configurations, we showed that mmWave MIMO system can enable Gbps data rates for infrastructure-to-vehicle communication in order to support the anticipated explosive rate demands of future ITS or NGVNs. Our direction for future work is to extend this work to the C-V2V scenario (for dual mobility) and the multi-user massive MIMO use case.

6 Acknowledgments

Sherif A. Busari and Kazi M.S. Huq would like to acknowledge their PhD and Post-doc grants funded by the Fundação para a Ciência e a Tecnologia (FCT-Portugal) with reference nos. PD/BD/113823/2015 and SFRH/BPD/110104/2015, respectively. This work is also funded by FCT/MEC through national funds under the project (THz-BEGUN), CMU/ECE/0013/2017.

7 References

[1] Qualcomm. '5G NR based C-V2X'. Available from: https://www.qualcomm.com/media/documents/files/5g-nr-based-c-v2x-presentation.pdf , accessed 14 January 2019

[2] Perfecto, C., Ser, J.D., Bennis, M.: 'Millimeter-Wave V2V Communications: Distributed Association and Beam Alignment', *IEEE J. Selected Areas Comm.*, 2017, **35**, (9), pp. 2148–2162

[3] Tonguz, O. K. 'How Vehicle-to-Vehicle Communication Could Replace Traffic Lights and Shorten Commutes'. IEEE Spectrum News, 2018. Available from: https://spectrum.ieee.org/transportation/infrastructure/how-vehicletovehicle-communication-could-replace-traffic-lights-and-shorten-commutes , accessed 14 January 2019

[4] Yang, G., Xiao, M., Poor, H.V.: 'Low-Latency Millimeter-Wave Communications: Traffic Dispersion or Network Densification?', *IEEE Trans. Comm.*, 2018, **66**, (8), pp. 3526–3539

[5] Va, V., Shimizu, T., Bansal, *et al.*: 'Millimeter Wave Vehicular Communications: A Survey', *Foundations and Trends in Networking*, 2016, **10**, (1), pp. 1–113

[6] Tassi, A., Egan, M., Piechocki, *et al.*: 'Modeling and Design of Millimeter-Wave Networks for Highway Vehicular Communication', *IEEE Trans. Veh. Tech.*, 2017, **66**, (12), pp. 10676–10691

[7] Yang, G., Xiao, M., Al.Zubaidy, *et al.*: 'Analysis of Millimeter-Wave Multi-Hop Networks With Full-Duplex Buffered Relays', *IEEE/ACM Trans. Netw.*, 2018, **26**, (1), pp. 576–590

[8] Busari, S. A., Huq, K. M. S., Mumtaz, S., *et al.*: 'Millimeter-Wave Massive MIMO Communication for Future Wireless Systems: A Survey', *IEEE Comm. Surv. & Tut.*, 2018, **20**, (2), pp. 836–869

[9] Busari, S. A., Mumtaz, S., Al.Rubaye, S., *et al.*: '5G Millimeter-Wave Mobile Broadband: Performance and Challenges', *IEEE Comm. Mag.*, 2018, **56**, (6), pp. 137–143

[10] Busari, S. A., Mumtaz, S., Huq, K. M. S., *et al.*: In: Shen, X. S., Lin, X., Zhang, K., Eds. 'Millimeter Wave Channel Measure'. Cham: Springer International Publishing, 2018 pp. 1–5. Available from: https://doi.org/10.1007/978-3-319-32903-1_115-1

[11] Xiao, M., Mumtaz, S., Huang, Y., *et al.*: 'Millimeter Wave Communications for Future Mobile Networks', *IEEE J. Selected Areas Comm.*, 2017, **35**, (9), pp. 1909–1935

[12] Mumtaz, S., Rodriguez, J., Dai, L., Eds. 'mmWave massive MIMO: A Paradigm for 5G'. (Academic Press, UK, 2017)

[13] Busari, S. A., Huq, K. M. S., Mumtaz, S., *et al.*: 'Impact of 3D Channel Modeling for Ultra-High Speed Beyond-5G Networks'. In: 2018 IEEE GLOBECOM Workshop on Ultra-high speed, low latency and massive connectivity communication for 5G/B5G. (Abu Dhabi, United Arab Emirates, 2018). pp. 1–6

[14] Va, V., Choi, J., Heath, R. W.: 'The Impact of Beamwidth on Temporal Channel Variation in Vehicular Channels and Its Implications', *IEEE Trans. Veh. Tech.*, 2017, **66**, (6), pp. 5014–5029

[15] Wang, Y., Venugopal, K., Molisch, A. F., *et al.*: 'Analysis of Urban Millimeter Wave Microcellular Networks'. In: 2016 IEEE 84th Veh. Tech. Conf. (VTC-Fall). 2016. pp. 1–5

[16] Kim, J., Chung, H., Noh, G., *et al.*: 'Field Trial of Millimeter-Wave-based MHN System for Vehicular Communications', *IET Conf. Proc.*, 2018, pp. 602 (5 pp.)–602 (5 pp.)(1). Available from: https://digital-library.theiet.org/content/conferences/10.1049/cp.2018.0961

[17] Wang, Y., Venugopal, K., Molisch, A. F., *et al.*: 'MmWave Vehicle-to-Infrastructure Communication: Analysis of Urban Microcellular Networks', *IEEE Trans. Veh. Tech.*, 2018, **67**, (8), pp. 7086–7100

[18] Gao, M., Ai, B., Niu, Y., *et al.*: 'Dynamic mmWave beam tracking for high speed railway communications'. In: 2018 IEEE Wireless Comm. & Netw. Conf. Workshops (WCNCW). 2018. pp. 278–283

[19] Cui, Y., Fang, X., Fang, Y., *et al.*: 'Optimal Nonuniform Steady mmWave Beamforming for High-Speed Railway', *IEEE Trans. Veh. Tech.*, 2018, **67**, (5), pp. 4350–4358

[20] 'Study on channel model for frequencies from 0.5 to 100 GHz, v14.3.0, 3GPP TR 38.901'. 2017. Available from: http://www.3gpp.org/ftp//Specs/archive/38_series/38.901 , accessed 14 January 2019

[21] Sun, S., MacCartney, G. R., Rappaport, T. S. 'A novel millimeter-wave channel simulator and applications for 5G wireless communications'. In: 2017 IEEE Int. Conf. Comm. (ICC 2017), pp. 1–7

[22] Rappaport, T. S., Sun, S., Shafi, M. 'Investigation and Comparison of 3GPP and NYUSIM Channel Models for 5G Wireless Communications'. In: 2017 IEEE 86th Veh. Tech. Conf. (VTC-Fall). 2017. pp. 1–5

[23] Choi, J., Va, V., Gonzalez.Prelcic, N., Daniels, R., Bhat, C.R., Heath, R.W.: 'Millimeter-Wave Vehicular Communication to Support Massive Automotive Sensing', *IEEE Communications Magazine*, 2016, **54**, (12), pp. 160–167

[24] Samimi, M. K., Rappaport, T. S.: '3-D Millimeter-Wave Statistical Channel Model for 5G Wireless System Design', *IEEE Trans. Microwave Theory and Techniques*, 2016, **64**, (7), pp. 2207–2225

[25] Busari, S. A., Huq, K. M. S., Felfel, G., *et al.*: 'Adaptive Resource Allocation for Energy-Efficient Millimeter-Wave Massive MIMO Networks'. In: IEEE GLOBECOM 2018, Abu Dhabi, UAE, pp. 1–6

[26] Goldsmith, A.: 'Wireless Communications'. Cambridge University Press, Cambridge, United Kingdom, 2005

[27] Buzzi, S., D'Andrea, C. 'On clustered statistical MIMO millimeter wave channel simulation', 2016. Available from: https://arxiv.org/abs/1604.00648.

[28] Shafi, M., Molisch, A. F., Smith, P. J., *et al.*: '5G: A Tutorial Overview of Standards, Trials, Challenges, Deployment, and Practice', *IEEE J. Selected Areas Comm.*, 2017, **35**, (6), pp. 1201–1221

[29] Zhang, J., Huang, Y., Yu, T., *et al.*: 'Hybrid Precoding for Multi-Subarray Millimeter-Wave Communication Systems', *IEEE Wireless Comm. Lett.*, 2018, **7**, (3), pp. 440–443

[30] Ayach, O.E., Rajagopal, S., Abu.Surra, S., Pi, Z., Heath, R.W.: 'Spatially Sparse Precoding in Millimeter Wave MIMO Systems', *IEEE Transactions on Wireless Communications*, 2014, **13**, (3), pp. 1499–1513

[31] Ai, B., Guan, K., He, R., *et al.*: 'On Indoor Millimeter Wave Massive MIMO Channels: Measurement and Simulation', *IEEE J. Selected Areas Comm.*, 2017, **35**, (7), pp. 1678–1690

[32] Mukherjee, S., Das, S. S., Chatterjee, A., Chatterjee, S.: 'Analytical Calculation of Rician K-Factor for Indoor Wireless Channel Models', *IEEE Access*, 2017, **5**, pp. 19194–19212

[33] Ju, S., Rappaport, T. S. 'Millimeter-wave Extended NYUSIM Channel Model for Spatial Consistency'. In: IEEE GLOBECOM 2018, Abu Dhabi, UAE, pp. 1–6

[34] Wang, C., Bian, J., Sun, J.,*et al.*: 'A Survey of 5G Channel Measurements and Models', *IEEE Comm. Surv. & Tut.*, 2018, **20**, (4), pp. 3142–3168

[35] Abdulgader, M. S. A., Wu, L. 'The Physical layer of the IEEE 802.11p WAVE Communication Standard: The Specifications and Challenges'. In: Proceedings of the World Congress on Engineering and Computer Science (WCECS). vol. II., San Fransisco, USA, 2014. pp. 1–8

[36] 'LTE Physical Layer Framework for Performance Verifcation, TSG RAN1 48, R1070674'. Available from: http://www.3gpp.org/DynaReport/TDocExMtg--R1-48--26033.htm , accessed 14 January 2019

[37] Busari, S. A., Mumtaz, S., Huq, K. M. S., *et al.*: 'System-Level Performance Evaluation for 5G mmWave Cellular Network'. In: IEEE GLOBECOM 2017, Singapore, pp. 1–7

[38] 3GPP. 'TS 38.211 Technical Specification Group Radio Access Network; NR, Physical channels and modulation v15.1.0'. (, . [Online]. Available from: http://www.3gpp.org/ftp//Specs/archive/38_series/38.211/ , accessed 14 January 2019